

Moderate resolution near-infrared spectroscopy of cool stars: a new *K*-band library

N. M. Förster Schreiber

Max-Planck-Institut für extraterrestrische Physik, Postfach 1312, D-85741 Garching, Germany
and
CEA/DSM/DAPNIA/Service d'Astrophysique, C.E. Saclay, F-91191 Gif sur Yvette CEDEX,
France

forster@discovery.saclay.cea.fr

ABSTRACT

I present an atlas of near-infrared *K*-band spectra of 31 late-type giants and supergiants, and two carbon stars. The spectra were obtained at resolving powers of 830 and 2000, and have a signal-to-noise ratio $\gtrsim 100$. These data are complemented with results from similar existing libraries in both *K*- and *H*-band, and are used to identify various tools useful for stellar population studies at moderate resolution. I focus on several of the most prominent absorption features and (1) investigate the effects of spectral resolution on measurements of their equivalent width (EW), (2) examine the variations with stellar parameters of the EWs, and (3) construct composite indices as indicators of stellar parameters and of the contribution from excess continuum sources commonly found in star-forming and AGN galaxies. Among the features considered, the ^{12}CO (2,0) and ^{12}CO (6,3) bandheads together with the Si I $1.59\ \mu\text{m}$ feature, first proposed by Oliva, Origlia, and coworkers, constitute the best diagnostic set for stellar spectral classification and for constraining the excess continuum emission. The Ca I $2.26\ \mu\text{m}$ and Mg I $2.28\ \mu\text{m}$ features offer alternatives in the *K*-band to the ^{12}CO (6,3) bandhead and Si I feature.

Subject headings: atlases — infrared: stars — stars: late-type — techniques: spectroscopic

1. Introduction

Among their many applications, libraries of stellar spectra are particularly useful in population and evolutionary synthesis of stellar clusters and galaxies. Extensive stellar databases now exist in the ultraviolet and optical regimes, and have been applied to numerous studies of Galactic and

extragalactic sources (*e.g.* Worthey 1994; Leitherer *et al.* 1996). These are, however, of limited usefulness for obscured systems. The near-infrared regime ($\lambda = 1 - 2.5 \mu\text{m}$) offers an alternative opportunity to probe obscured sources since extinction effects are much less important at these wavelengths (*e.g.* $A_{2.2\mu\text{m}} \approx 0.1 A_V$). In addition, cool ($\sim 3000 - 6000 \text{ K}$) stellar populations are best studied in the near-infrared because their spectral energy distributions peak near $1 \mu\text{m}$.

Since the pioneering work of Johnson & Méndez (1970), and especially in the past decade due to improvements in instrumentation and detector sensitivity, many investigators have conducted near-infrared spectroscopic studies of stars, covering overall wide ranges in stellar types and spectral resolution (see *e.g.* Origlia, Moorwood, & Oliva 1993, Wallace & Hinkle 1997, and Meyer *et al.* 1998 for reviews). A number of atlases at moderate resolving powers in the *H*- and *K*-band ($\lambda = 1.45 - 1.85 \mu\text{m}$ and $\lambda = 1.9 - 2.5 \mu\text{m}$ respectively) have been assembled, sampling various types of cool stars more systematically, and intended for spectral classification and population synthesis purposes. The first such library was provided by Kleinmann & Hall (1986, hereafter KH86), and was followed notably by the work of Lançon & Rocca-Volmerange (1992), Origlia *et al.* (1993, OMO93), Ali *et al.* (1995), Dallier, Boisson, & Joly (1996, DBJ96), Ramírez *et al.* (1997), Wallace & Hinkle (1997), Lançon & Wood (1998), and Meyer *et al.* (1998). Some of these authors interpreted their data together with theoretical stellar atmosphere models as well as with observations of template composite populations to better understand the dependence of key spectral features on stellar parameters (*e.g.* OMO93; Ali *et al.* 1995; Origlia *et al.* 1997; Oliva & Origlia 1998). Lançon and her co-workers implemented their empirical library in evolutionary synthesis codes to model stellar clusters and galaxies (Lançon & Rocca-Volmerange 1996; Lançon *et al.* 1999).

Despite these contributions, additional efforts would be beneficial to improve the quality and consistency of quantitative diagnostic tools suitable for stellar population studies. Specific problems include the disparity in spectral resolution of the various atlases, and the different definitions of spectroscopic indices used to quantify the strength of the stellar absorption features. Some studies targeted specific regions of the Hertzsprung-Russell diagram while others aimed at a larger coverage but with coarser sampling. Altogether, the existing libraries relevant for cool stars constitute a rather heterogeneous data set.

In this context, I have assembled a new near-infrared stellar library obtained with the Max-Planck-Institut für extraterrestrische Physik (MPE) 3D instrument (Weitzel *et al.* 1996). It is intended at widening existing libraries primarily for applications to extragalactic studies. The 3D atlas includes normal late-type giants and supergiants as well as asymptotic giant branch — or AGB — stars, which usually dominate the near-infrared continuum emission of galaxies (*e.g.* Bruzual & Charlot 1993). In this paper, I present *K*-band spectra at $R \equiv \lambda/\Delta\lambda \approx 830$ and 2000 with signal-to-noise ratio $S/N \gtrsim 100$ of 31 giants and supergiants mostly with near-solar abundances, and of two representative carbon stars. In order to obtain a larger and, ultimately, an homogeneous data set, the 3D sample is augmented with data from similar libraries in the *H*- and *K*-band selected from the literature. I focus on several of the most prominent absorption features,

investigate the effects of spectral resolution on measurements of their equivalent widths (EWs), and compile consistently the results from the different data sets. I use the data to identify diagnostics of the stellar population composition and of excess continuum emission (such as due to hot dust heated by OB stars or by an AGN). Additional spectra in the H -band and of AGB stars will be presented and analyzed in future contributions.

The paper is organized as follows. I describe the selection of the program stars, the observations, and the data reduction in section 2. In section 3, I present the results, investigate the effects of spectral resolution on the EWs, and augment the 3D data set with EWs obtained from selected existing atlases. In section 4, I discuss the variations of the EWs with stellar parameters and explore various composite spectroscopic indices. The paper is summarized in section 5.

2. Selection, observations and data reduction of the 3D sample

2.1. Selection of program stars

Table 1 lists the program stars, their spectral types, and their metallicities from three literature sources (McWilliam 1990; Taylor 1991; Cayrel de Strobel *et al.* 1992). The sample includes 25 giants (luminosity class III) and six supergiants (luminosity classes I and II) of late-G, K, and M types. They were selected from the list of optical spectral standards and well-classified stars of Keenan & McNeil (1989), and two additional stars were taken from Cayrel de Strobel *et al.* (1992). The spectral types are given in the revised MK system (Keenan 1987) and were cross-checked with Keenan & Yorke (1988), Garrison (1994), Keenan & Pitts (1980), and Morgan & Keenan (1973). Stars belonging to double or multiple systems were excluded in the selection. Except for a few giants with $[\text{Fe}/\text{H}] < -0.3$, none of the stars are known to have strong abundance anomalies. In addition, one N-type and one early-R type carbon stars drawn from the sample of Yamashita (1972) were observed. The spectral types assigned by Yamashita in the C-classification scheme of Keenan & Morgan (1941) are given, as well as those he quotes in the R- and N-system used in the Henry Draper Catalogue (*e.g.* Shane 1928).

2.2. Observations

The stars were observed using the MPE near-infrared integral field spectrometer 3D (Weitzel *et al.* 1996). A first set of spectra was obtained at the 3.5 m telescope in Calar Alto, Spain, on 1995 January 12, 18, and 20. A second set was collected at the 4.2 m William-Herschel-Telescope in La Palma, Canary Islands, on 1996 January 2 and 9. The observations were completed at the 2.2 m ESO telescope in La Silla, Chile, between 1996 April 10 and 20. 3D images a square field of view at $0.3'' - 0.5''$ per pixel and provides simultaneously the H - or K -band spectrum of each spatial pixel. The focal plane is sliced in 16 parallel “slits” whose light is dispersed in wavelength by a grism onto

a 256×256 HgCdTe NICMOS 3 array. The data are rearranged in a three-dimensional cube during data processing. The intrinsic spectral sampling of 3D is with pixels of size λ/R ; Nyquist-sampled spectra are achieved by dithering the sampling by half a pixel on alternate data sets which are interleaved in wavelength (“merged”) during data reduction. The Calar Alto and La Palma data were obtained at $R \approx 830$ in the range $\lambda = 1.9 - 2.4 \mu\text{m}$ and the La Silla data, at $R \approx 2000$ between $2.18 \mu\text{m}$ and $2.45 \mu\text{m}$.

Each star was observed in two sequences of several exposures, each sequence taken with spectral sampling shifted by half a pixel with respect to the other. Two similar sequences were obtained at off-source positions at most $1'$ away from the stars. To further minimize the effects of variable background emission, the on- and off-source sequences were alternated on timescales of less than 10 minutes. The integration time and number of individual exposures were dictated by the brightness of each star and by the requirement of achieving a $S/N \gtrsim 100$ per wavelength channel. For atmospheric calibration, B, A, F, and early-G type stars were observed each night, before and after the program stars. Reference stars close to the library stars were chosen to optimize the correction for differential airmass and transmission spectrum. Each night, images were taken of the observatory’s dome and of a glowing Nernst rod for spatial and spectral flat-fielding, as well as of a neon discharge lamp for wavelength calibration. Table 2 gives the log of the observations.

2.3. Data reduction

The data reduction was carried out using the 3D data analysis package, within the GIPSY environment (van der Hulst *et al.* 1992). The basic steps were performed following standard procedures as described in Weitzel *et al.* (1996). These include correction for the non-linear signal response of the detector, averaging of single-frame exposures, dark current and background subtraction, flat-fielding, wavelength calibration, spectral redistribution onto a regular grid and merging, rearrangement of the data in a three-dimensional cube, and correction for bad and hot pixels. Residuals due to spatial and temporal variations in the background emission level are $\lesssim 1\%$.

The atmospheric transmission was corrected for with the help of the reference stars data reduced in the manner described above. The calibration spectra extracted from the data cubes were divided by a black-body curve of appropriate temperature given the spectral type of each reference star. The intrinsic absorption features of the late-F and early-G dwarf calibrators were corrected for by division with the normalized spectrum of the G3 V star from the KH86 atlas, convolved with a gaussian profile to the resolution of the 3D data. This template star has similar line strengths as the calibrators except for the $\text{Br}\gamma$ absorption at $2.166 \mu\text{m}$, which was removed by linear interpolation. The B- and A-type calibrators are expected to be featureless at $R \sim 830 - 2000$ apart from $\text{Br}\gamma$ absorption, again removed by linear interpolation. The exception is the A8 Ib calibrator used for HD 78647, which likely has absorption from the Pfund series of hydrogen longwards of $2.32 \mu\text{m}$ (see Wallace & Hinkle 1997 who detected these lines in A through early-F supergiants at $R \sim 3000$). In the final spectrum of HD 78647, corresponding residuals are however not obvious.

The final spectra of the program stars were extracted from the data cubes after division by the calibration spectra. The residuals from intrinsic features of the reference stars are $\leq 1\%$. Those due to spatial and temporal variations of atmospheric transmission could be further reduced using synthetic spectra of the differential transmission generated with the program ATRAN (Lord 1992) and by adjusting the zenithal distances and water vapour column densities assigned to the library and reference stars. Telluric features do not persist to more than 1% in most of the band, and 5% around $2.0\ \mu\text{m}$ (10% for HD 25025).

At the higher spectral resolution for the La Silla observations, and more importantly for the $0.3''\ \text{pixel}^{-1}$ scale used for several stars, a complex high-frequency interference pattern appeared in the data, due to multiple reflections at the surface of the detector array. The frequency and position angle of the fringes varied with position on the array and with wavelength sampling, and differed significantly for defocussed observations (*e.g.* in the dome images). This pattern multiplicatively modulated the observed counts with a typical peak-to-peak amplitude of 5% – 10%. The similar nature of the program and reference sources as well as of the technical conditions under which they were observed (telescope pointing close to the zenith, same focus, source positioned at the center of the array) resulted in nearly identical interference patterns in the respective data sets. The division of the library stars data by the calibration spectra cancelled the fringes to better than 1% except for HD 82668, where they remained at the 3% level at short wavelengths.

The final uncertainties in spectral flux distribution of the reduced data are estimated to be less than 3% – 4% at $\lambda > 2\ \mu\text{m}$, and $\leq 10\%$ near and shortwards of $2\ \mu\text{m}$. They include possible systematic errors which may occur in the background subtraction, in the merging of the wavelength-shifted data sets, in the correction for telluric transmission and intrinsic features of the reference stars, and residuals from the interference pattern in the higher resolution data. As an indication of the quality of the final spectra, an effective S/N ratio was evaluated on the reduced data between $2.242\ \mu\text{m}$ and $2.258\ \mu\text{m}$. It was taken as the inverse of the standard deviation about the mean flux after division by a straight line fitted over this range; the values are reported in table 2. This estimated S/N ratio is intended at providing a measure of the effective, resultant noise over a relatively line-free portion of the fully reduced spectra, near the various absorption features discussed in this paper. For the N-type carbon star HD 92055, it is however affected by the presence of significant intrinsic absorption features in the range considered (see section 3.1 below).

3. Results

3.1. 3D spectra

The spectra are plotted in figures 1 and 2, sorted according to luminosity class and advancing spectral type. They are normalized to unity in the interval $\lambda = 2.2875 - 2.2910\ \mu\text{m}$ and presented on a linear flux scale, vertically shifted by equal intervals of 0.5 starting at the bottom. The considerable continuum structure is most obvious in the higher resolution spectra of figure 2. The

variation in strength of most features with spectral type and luminosity class is also apparent. The strongest features longwards of $2.15\ \mu\text{m}$ for the normal giants and supergiants were identified by comparing their locations with those given in KH86. As shown by Wallace & Hinkle (1996) based on $R \geq 45000$ spectra, the atomic features result from the blending of lines from multiple species (see section 4.1). The nomenclature of KH86 is adopted here to keep with the convention established so far. Wallace & Hinkle (1996) also identified numerous lines of the CN red system shortwards of $2.29\ \mu\text{m}$ and, in the latest M-types, of H_2O as well. At moderate resolution, the blending of these lines produce the low-level “grass-like” continuum structure (see also Wallace & Hinkle 1997).

For the two carbon stars, the CO first overtone bandheads are easily recognized as the most prominent features in the 3D spectra. Figure 3 compares the spectra of the carbon stars with those of normal giants of similar effective temperature (see section 3.4 below). HD 92055 (C6,3 – N2) exhibits similar CO bandhead strengths as HD 80431 (M4 III) but substantially more continuum structure at shorter wavelengths. In the K -band spectrum of N-type carbon stars, believed to lie on the thermally-pulsing AGB (see Wallerstein & Knapp 1998, and references therein), lines from the CN red system and perhaps some lines of the C_2 Phillips system become conspicuous, hiding less prominent atomic features (*e.g.* Wallace & Hinkle 1996; Lançon & Wood 1998). On the other hand, early-R stars are presumably in earlier evolutionary stages and their atmospheres seem to behave as those of normal K giants, but their nature remains unknown (*e.g.* Wallerstein & Knapp 1998). The spectrum of HD 113801 (C2,1 – R0) is almost identical to that of its temperature counterpart HD 107328 (K0.5 IIIb), suggesting common dominant sources of opacity for the strongest features, with carbon star features too weak to be detected at moderate resolution.

The quality of the 3D data is illustrated in figure 4, which compares several of the higher-resolution spectra with those for similar spectral types from KH86, convolved to $R \sim 2000$ with a gaussian profile. The original KH86 spectra have $R \sim 3000$ and $\text{S/N} \sim 100 - 1000$, and are ratioed with A0 V stars. In order to recover the original energy distributions, they were multiplied by a power-law continuum $\propto \lambda^{-3.94}$ which is the closest representation of an A0 dwarf (Kurucz 1979, as quoted by McGregor 1987). In all cases, the 3D and KH86 data compare remarkably well.

3.2. Definition of equivalent widths

The strength of absorption features was quantified by the equivalent width (EW), defined as:

$$W_\lambda = \int_{\lambda_1}^{\lambda_2} (1 - f_\lambda) d\lambda, \quad (1)$$

where f_λ is the spectrum normalized to a flat continuum slope while λ_1 and λ_2 are the integration limits, and $d\lambda$ is expressed in \AA . EWs are independent of extinction since the effects of continuous opacity of interstellar dust grains are cancelled by the continuum normalization. The EWs were measured for the features involving the Na I doublet centered at $2.2076\ \mu\text{m}$ and the Ca I multiplet

centered at $2.2636 \mu\text{m}$, and for the $^{12}\text{CO} (2,0)$, $^{12}\text{CO} (3,1)$, and $^{13}\text{CO} (2,0)$ first overtone bandheads at $2.2935 \mu\text{m}$, $2.3227 \mu\text{m}$, and $2.3448 \mu\text{m}$ respectively (hereafter W_{Na} , W_{Ca} , $W_{2.29}$, $W_{2.32}$, and $W_{2.34}$). In addition, the EWs of the features involving the Fe I lines at $2.2263 \mu\text{m}$ and $2.2387 \mu\text{m}$, and the Mg I line at $2.2814 \mu\text{m}$ (W_{Fe1} , W_{Fe2} , W_{Mg}) were measured in the higher resolution spectra.

To avoid complications if the continuum shape is distorted by broad absorption features, such as those due to H_2O around $1.9 \mu\text{m}$ and $2.7 \mu\text{m}$ in the coolest stars, or affected by extinction and contributions from emission sources such as hot dust, the local continuum was preferred for most features. The normalizing continuum for each atomic feature was obtained by linear interpolation between adjacent regions $0.002 - 0.003 \mu\text{m}$ wide on each side of the absorption. Since there is no line-free continuum redwards of $2.3 \mu\text{m}$ in the 3D spectra, the normalizing continuum for the CO bandheads was defined at short wavelengths only. For $^{12}\text{CO} (2,0)$, it was taken as the average in the clear band around $2.29 \mu\text{m}$. Although the continuum slope is thereby not constrained, this does not introduce large uncertainties in $W_{2.29}$ because the feature bandpass is narrow and close enough to the continuum interval. In the case of $^{12}\text{CO} (3,1)$ and $^{13}\text{CO} (2,0)$, a power-law was fitted to featureless regions between $2.21 \mu\text{m}$ and $2.29 \mu\text{m}$ to better extrapolate over the bandheads.

The narrow bands used in the computation of the EWs are reported in table 3. The integration limits for the Na I and Ca I features and the CO bandheads, as well as the continuum definition for $^{12}\text{CO} (2,0)$ are as in KH86. The definition of $W_{2.29}$ is also the same as used by OMO93. In view of the compilation of selected data sets from the literature below, the definition of the local continuum and bandpass edges adopted by OMO93 to measure the EW of the $^{12}\text{CO} (6,3)$ second overtone bandhead at $1.6187 \mu\text{m}$ and the Si I feature at $1.5892 \mu\text{m}$ ($W_{1.62}$ and $W_{1.59}$) are also listed.

3.3. Effects of spectral resolution

In order to provide a means for comparing results from data obtained at different spectral resolution or affected by velocity broadening, the variations of the EWs defined above with instrumental resolution were investigated. The Mg I and Fe I features were excluded from this analysis because their weakness hampers reliable measurements at $R \lesssim 1000$. The instrumental profiles were represented by gaussian functions.

Grids of spectra convolved with gaussians corresponding to velocity dispersions σ ranging from 0 km s^{-1} to 400 km s^{-1} , in steps of 10 km s^{-1} , were generated using the KH86 spectra ($R \sim 3000$) for types later than K0, and the 3D spectra at $R \approx 2000$. The variations of the EWs with σ did not depend on the chosen templates and were best fitted by second order polynomials. Velocity dispersions $\sigma < 60 \text{ km s}^{-1}$ for the CO bandheads, and $\sigma < 20 \text{ km s}^{-1}$ for the Na I and Ca I features produced no measurable effect. The scatter around the fits was less than $\pm 5\%$ for $\sigma \leq 200 \text{ km s}^{-1}$ but increased for larger σ , corresponding to $R \lesssim 600$. Since at such resolving powers, the resolution element λ/R becomes comparable to the integration intervals $\lambda_2 - \lambda_1$, $\sigma \leq 200 \text{ km s}^{-1}$ is considered as the range of validity for the empirical corrections.

Oliva *et al.* (1995) used this approach to derive corrections for $W_{1.59}$, $W_{1.62}$, and $W_{2.29}$ measured in velocity broadened spectra. Their correction for $W_{2.29}$ obtained using templates at $R \sim 2500$ is given by a linear relationship for $\sigma \geq 60 \text{ km s}^{-1}$. Within the dispersion of the results, this line approximates well the fit obtained here in the range $\sigma = 60 - 200 \text{ km s}^{-1}$ and is adopted for consistency with previous work. The empirical relationships including those for the H -band features from Oliva *et al.* are the following, where W_{λ}^{obs} denotes the observed EW. For $W_{1.59}$, $W_{1.62}$, and $W_{2.29}$,

$$W_{\lambda} = W_{\lambda}^{\text{obs}} [1 + a_{\lambda} (\sigma - 60)] \quad (2)$$

for $60 \text{ km s}^{-1} \leq \sigma \leq 200 \text{ km s}^{-1}$

where $a_{1.59} = 8.70 \times 10^{-4}$, $a_{1.62} = 7.10 \times 10^{-4}$, and $a_{2.29} = 8.75 \times 10^{-4}$; for $W_{2.32}$ and $W_{2.34}$,

$$W_{\lambda} = W_{\lambda}^{\text{obs}} \left[1 + a_{\lambda} (\sigma - 60) + b_{\lambda} (\sigma - 60)^2 \right] \quad (3)$$

for $60 \text{ km s}^{-1} \leq \sigma \leq 200 \text{ km s}^{-1}$

where $a_{2.32} = 4.38 \times 10^{-4}$, $b_{2.32} = 3.52 \times 10^{-6}$, $a_{2.34} = 1.32 \times 10^{-4}$, and $b_{2.34} = 2.61 \times 10^{-6}$; and for W_{Na} and W_{Ca} ,

$$W_{\lambda} = W_{\lambda}^{\text{obs}} \left[1 + a_{\lambda} (\sigma - 20) + b_{\lambda} (\sigma - 20)^2 \right] \quad (4)$$

for $20 \text{ km s}^{-1} \leq \sigma \leq 200 \text{ km s}^{-1}$

where $a_{\text{Na}} = 1.67 \times 10^{-3}$, $b_{\text{Na}} = 4.43 \times 10^{-6}$, $a_{\text{Ca}} = 2.33 \times 10^{-4}$, and $b_{\text{Ca}} = 6.24 \times 10^{-6}$. The corrections for $R \sim 1000$ amount to $\approx 5\%$ or less except for W_{Ca} (10%) and W_{Na} (22%). At $R \sim 600$, they are $\approx 13\%$ or less, 27%, and 48% respectively.

3.4. Compilation of data from 3D and additional selected atlases

The EWs measured on the 3D spectra, corrected for resolution where appropriate, are listed in table 4. The atomic features were not measured for the carbon stars. The atlases of KH86, OMO93, and DBJ96 were chosen to complement the 3D library, providing a larger database. These data sets include H - and K -band spectra at $R \sim 1500 - 3000$. The EWs were measured on the digitally available spectra of DBJ96 and KH86; the EWs given in OMO93 were taken directly because measured according to the definitions adopted here. Corrections for instrumental resolution were applied where appropriate. Formal uncertainties were derived from the rms noise in the spectra and propagating this uncertainty through Eq. 1; average values ranged between 0.1 \AA and 0.2 \AA . The continuum placement introduces larger uncertainties which were estimated by varying slightly the continuum-defining intervals, resulting in about 1% – 2% error in the continuum level. The final measurement uncertainties adopted are $\pm 0.5 \text{ \AA}$ for the atomic features and $W_{1.62}$, $\pm 0.8 \text{ \AA}$ for $W_{2.29}$, and $\pm 1.0 \text{ \AA}$ for $W_{2.32}$ and $W_{2.34}$.

The variations of the EWs with stellar effective temperature (T_{eff}) are shown in figure 5. The spectral types were converted to temperatures using the calibrations for late-type stars of Schmidt-Kaler (1982). For the carbon stars, individual determinations were adopted: $T_{\text{eff}} = 4700$ K for HD 113801 (Dominy 1984) and 3080 K for HD 92055 (Ohnaka & Tsuji 1996). The EWs for main-sequence stars from KH86 and DBJ96 are included for comparison purposes. The data obtained from the various references are in excellent agreement. No systematic deviation of a particular data set is seen and for the few stars common to two or more samples, the EWs agree within the measurement uncertainties.

4. Discussion

4.1. Variations of selected features with stellar parameters

As can be seen from figure 5, the absorption features of interest in cool, evolved stars vary strongly with T_{eff} over the range of spectral types considered, except for Si I and Mg I. The first overtone CO bandheads show the long recognized trend with luminosity class for $T_{\text{eff}} \leq 4500$ K, supergiants exhibiting deeper bandheads than giants of the same temperature. A similar trend is seen below 4000 K for the Na I and both Fe I features. The K -band EWs in supergiants seem to decrease more rapidly at $T_{\text{eff}} \geq 4500$ K than those in giants but this needs to be confirmed with additional data given the poor sampling in the range 4500 – 6000 K at high luminosity. The giants generally form a tight distribution in the EW versus T_{eff} diagrams whereas the supergiants display a larger scatter. This is presumably due to the larger uncertainties in the T_{eff} calibration and spectral type assignment, and the larger range in luminosity within classes I/II (*e.g.* Humphreys & McElroy 1984).

No metallicity effect is obvious in the data presented here, mainly because of the limited range in $[\text{Fe}/\text{H}]$ covered by most stars in the samples and the fairly large uncertainties in $[\text{Fe}/\text{H}]$ determinations (see table 1). From previous empirical and theoretical studies, a variation of the EWs is expected at more extreme metallicities, with an increase from low to high $[\text{Fe}/\text{H}]$ (*e.g.* Frogel *et al.* 1978; Frogel, Cohen, & Persson 1983; Terndrup, Frogel, & Whitford 1991; Ali *et al.* 1995; Origlia *et al.* 1997; Oliva & Origlia 1998; Stephens, Frogel, & Ramírez 2000). Part of the dispersion of the data probably reflects the small differences in $[\text{Fe}/\text{H}]$ in addition to small variations in intrinsic T_{eff} and other parameters among stars of a given spectral type.

The dwarfs are clearly distinguished by lower EWs for $T_{\text{eff}} \leq 4000 - 4500$ K, except for Na I and Mg I. The uncertain chemical composition of the coolest dwarfs from KH86 (especially for the M2+ V star which may belong to the halo population) prevent further interpretation here. More details on dwarfs can be found in Ali *et al.* (1995), DBJ96, Ramírez *et al.* (1997), and Meyer *et al.* (1998). The EWs for the first overtone CO bandheads measured in both carbon stars lie on the loci defined by the normal red giants but, obviously, no conclusion pertaining to these particular types can be drawn from such a limited sample. Alvarez *et al.* (2000) found from a larger sample

that carbon-rich AGB stars exhibit the full range in CO bandhead strength observed for cool, oxygen-rich evolved stars, including supergiants. In the rest of this paper, the discussion of EWs and combinations thereof focusses on normal red giants and supergiants.

The behaviours of the various features with spectral type and luminosity class seen in figure 5 have been amply discussed in the literature cited in this work. It is important to emphasize that the discussion here is intended at identifying empirical indicators useful for spectral classification and population synthesis. A detailed physical interpretation is beyond the scope of this paper; efforts have been made in that sense by *e.g.* McWilliam & Lambert (1984), OMO93, and Ali *et al.* (1995). Such an interpretation is far from trivial because of the contributions of lines of various species within the bandpasses used to measure the features and the continuum at moderate resolution. In addition, other relevant parameters have to be accounted for, such as the surface gravity, the detailed chemical composition, and the micro-turbulence velocity.

As an illustration, figure 6 shows the line identifications of Wallace & Hinkle (1996) in their $R \geq 45000$ spectra of late-type stars within the bandpasses used in this work to quantify the atomic features in the K -band. Compared to the molecular features, they are more “contaminated,” and include contributions from Sc I, Ti I, V I, Si I, S I, and HF (1,0) lines. In particular, the variations with temperature and luminosity of the Na I, Ca I, and Fe I features seem primarily governed by Sc I, Ti I, and V I, which may even become the dominant sources of absorption in the coolest giants and supergiants. As noted by Wallace & Hinkle (1996), the identifications adopted by KH86 are more appropriate for dwarfs than for giants and supergiants, not surprisingly because they were based on the comparison of the spectrum of the K5 V star 61 Cyg A with those of sunspots.

4.2. Stellar temperature and luminosity indicators

Several empirical diagnostics of spectral type and luminosity class can be identified from the EWs discussed above. Due to the restricted range in metallicities of the stellar samples, these tools are valid for populations with near-solar abundances.

The $W_{1.62}$ and W_{Ca} constitute pure T_{eff} indicators. None of the absorption features discussed here varies strictly with luminosity class, so distinguishing giants from supergiants requires combining T_{eff} -sensitive EWs, including at least one also sensitive to luminosity class. The most sensitive luminosity indicator is $W_{2.29}$. The $W_{2.29}/W_{2.32}$ and $W_{2.29}/W_{2.34}$ ratios plotted in figure 7 show that all three EWs carry nearly the same information about the spectral type and luminosity class for giants and supergiants (the sharp increase of $W_{2.29}/W_{2.34}$ at temperatures above 4500 K may be an artefact due to the extreme weakness of the ^{13}CO (2,0) bandhead). For the coolest stars ($T_{\text{eff}} \lesssim 4000$ K) and with sufficient S/N ratio measurements, W_{Na} , W_{Fe1} , and W_{Fe2} also discriminate between luminosity classes III and I/II.

Various combinations of EWs (sums and ratios) were explored as possible temperature and luminosity indicators. In most cases, the composite indices displayed too large a scatter to provide

better diagnostics than single EWs alone. However, a few proved to be potentially useful and are shown in figure 7. As demonstrated by OMO93, $\log(W_{1.62}/W_{1.59})$ and $\log(W_{1.62}/W_{2.29})$ are sensitive T_{eff} indicators, and the former is not affected by a luminosity dependence. The $W_{2.29}/W_{\text{Mg}}$ ratio has a pronounced temperature sensitivity, mostly due to $W_{2.29}$, but the number of data points is smaller and the scatter is larger than for $\log(W_{1.62}/W_{1.59})$. The sum of W_{Fe1} and W_{Fe2} provides a higher S/N ratio measurement than the individual EWs, and a temperature diagnostic with luminosity sensitivity below 4000 K. Combining the sharp increase of $W_{2.29}$ and W_{Ca} with decreasing T_{eff} and the luminosity sensitivity of $W_{2.29}$ results in a $W_{2.29}/W_{\text{Ca}}$ ratio distinguishing giants from supergiants at $T_{\text{eff}} \lesssim 4500$ K. Ramírez *et al.* (1997) showed that the ratio of $W_{2.29}$ and $(W_{\text{Ca}} + W_{\text{Na}})$ constitutes a very good discriminator between giants and dwarfs below 4800 K, independent of T_{eff} ¹. As can be seen in figure 7, it is however less powerful than $W_{2.29}/W_{\text{Ca}}$ for differentiating giants from supergiants because of the luminosity sensitivity of W_{Na} . Due to similar behaviours with T_{eff} and luminosity class of $W_{2.29}$ and W_{Na} , their ratio is in fact essentially identical in giants and supergiants (not shown in figure 7).

4.3. Contamination by excess continuum sources

The interpretation of the EWs becomes more intricate in objects where additional continuum sources contribute to the near-infrared emission. In particular, emission from small interstellar dust grains heated at $T \sim 1000$ K by OB stars or by an AGN, photospheric emission from hot stars, or nebular free-free and free-bound emission may “dilute” the absorption features due to the cool stars in star-forming and AGN galaxies. In this case, the properties of the cool stellar population can be determined from the relative strength of features close enough in wavelength to be affected by similar amounts of dilution, making the ratio of their EWs insensitive to such effects. In addition, the combination of dilution-free indicators with diluted EWs allows one to estimate the excess continuum emission without requiring any knowledge about the properties of the sources, which are usually very uncertain.

Oliva *et al.* (1995) proposed $\log(W_{1.62}/W_{1.59})$ as a dilution-free temperature indicator, and used it in combination with $W_{1.62}$ and $\log(W_{1.62}/W_{2.29})$ to constrain the amount of dilution around $1.6 \mu\text{m}$ and $2.3 \mu\text{m}$ in various types of galaxies. For this purpose, they used spectroscopic equivalents of colour-magnitude plots, namely the $W_{1.62}$ versus $\log(W_{1.62}/W_{1.59})$ and $W_{1.62}$ versus $\log(W_{1.62}/W_{2.29})$ diagrams, reproduced in figure 8. In these diagrams, composite stellar populations whose near-infrared emission is undiluted occupy regions falling on the observed distributions for individual stars. The amount of dilution near $1.6 \mu\text{m}$ is determined from the vertical displacement with respect to the locus of stars in the $W_{1.62}$ versus $\log(W_{1.62}/W_{1.59})$ diagram. Similarly, the amount of dilution near $2.3 \mu\text{m}$ is estimated from the horizontal displacement in the $W_{1.62}$ versus

¹Ramírez *et al.*’s EWs are measured differently, but the conclusions are the same with the definitions adopted here and the EWs for dwarfs measured on the KH86 spectra.

$\log (W_{1.62}/W_{2.29})$ diagram, once the $W_{1.62}$ has been corrected for dilution. However, because giants and supergiants lie on separate branches in the latter plot, two solutions for the $2.3\ \mu\text{m}$ dilution are possible unless the luminosity class can be constrained independently.

Similar diagrams constructed strictly from the K -band data are less satisfactory mainly because of larger scatter and/or lack of strong enough temperature dependence in ratios of EWs. Furthermore, the variation with luminosity class of almost all indices at low temperatures may introduce degeneracy in the determination of the amount of dilution. The best diagrams in terms of smaller scatter are W_{Ca} versus $W_{2.29}/W_{\text{Mg}}$ and $W_{2.29}$ versus $W_{2.29}/W_{\text{Mg}}$, also shown in figure 8. The $W_{2.29}/W_{\text{Mg}}$ ratio constitutes the dilution-free temperature indicator while W_{Ca} and $W_{2.29}$ are potentially affected by dilution, which can then be estimated from the vertical displacement relative to the distribution of stars. The W_{Ca} versus $W_{2.29}/W_{\text{Mg}}$ diagram would in principle be superior because both indices are only sensitive to T_{eff} , yielding an unambiguous solution for the dilution. However, the relatively loose distribution of the data limits the accuracy. The $W_{2.29}$ versus $W_{2.29}/W_{\text{Mg}}$ diagram exhibits the characteristic double-branch behaviour of other similar diagrams due to luminosity effects. The difference in dilution inferred assuming a population of supergiants instead of giants can amount to 50% for very cool populations.

4.4. Applications to stellar population studies

Applications of the diagnostic tools discussed in this paper to studies of stellar clusters and galaxies have shown their usefulness for constraining the composition of evolved stellar populations and the amount of excess continuum emission (*e.g.* Oliva *et al.* 1995; Böker, Förster Schreiber, & Genzel 1997; Thatte *et al.* 1997; Oliva *et al.* 1999; Förster Schreiber *et al.* 2000a). Implemented in evolutionary synthesis models, they can also provide quantitative constraints on the star formation history (*e.g.* Origlia & Oliva 2000; Förster Schreiber *et al.* 2000b).

In applying these tools, it is however important to bear in mind some of their potential limitations, briefly outlined here. The frequently limited S/N ratio for extragalactic sources may hamper reliable measurements of weak features. The dispersion in the template stellar data alone limits the accuracy in determinations of T_{eff} and of the dilution. This depends on the chosen diagnostics as well as the actual T_{eff} range and luminosity class of the stars under consideration, but typical uncertainties are of about ± 250 K for T_{eff} (or about ± 3 spectral sub-classes within K- and M-types) and of $\approx 10\% - 20\%$ for the dilution. Degeneracy between luminosity class and dilution may lead to two possible solutions for these properties. The interpretation of the feature strengths is further complicated when distinct cool populations contribute to the integrated emission, such as red supergiants formed in a recent starburst and older, preexisting giants. Finally, predictions of the variations with time of the EWs using evolutionary synthesis models can be affected by additional uncertainties which arise notably from the possible inadequacy of current stellar tracks to represent the evolution of intermediate-mass stars along the AGB (*e.g.* Origlia & Oliva 2000) — not mentioning the scarcity of data for AGB stars.

The various indicators remain nonetheless valuable tools for extragalactic applications as specific probes of the cool, evolved stars. In cases where their diagnostic power is limited, they benefit to be complemented with additional constraints also sensitive to the stellar contents such as the mass-to-light ratio, or with the spatial distribution of the EWs and of the stellar near-infrared continuum emission which can provide indirect evidence concerning the nature of the stellar population at a given location (*e.g.* Oliva *et al.* 1999; Förster Schreiber *et al.* 2000a).

5. Summary

K -band spectra at $R \approx 830$ and 2000 of 31 late-type giants and supergiants mostly with near-solar abundances, and of two carbon stars were obtained with the aim of widening existing near-infrared stellar libraries useful for population synthesis of clusters and galaxies. The EWs of several of the most prominent absorption features were computed: the Na I 2.2076 μm and Ca I 2.2636 μm features, and the ^{12}CO (2,0), ^{12}CO (3,1), and ^{13}CO (2,0) bandheads. Relationships between these EWs and the instrumental resolution were derived. These allow comparison between data sets obtained with different resolving powers in the range $R \sim 600 - 3000$ or, equivalently, affected by velocity broadening up to $\sigma = 200 \text{ km s}^{-1}$. In addition, the EWs of the Mg I 2.2814 μm , Fe I 2.2263, and Fe I 2.2387 μm features were measured in the higher resolution spectra.

The 3D data set was augmented with EWs obtained from other similar stellar libraries, and complemented with EWs of the ^{12}CO (6,3) bandhead and Si I 1.5892 μm feature in the H -band. This extended database was used to investigate spectroscopic diagnostics of stellar spectral type and luminosity class as well as of the contribution by excess continuum sources. The main conclusions are the following.

- The various data sets compare remarkably well. Compiled together, they better constrain the variations of the absorption features with spectral type and luminosity class found previously by various authors based on smaller samples.

- Several features provide useful tools in population studies of stellar clusters and galaxies. Among the EWs considered, $W_{2.29}$, $W_{1.62}$ and $W_{1.59}$ first proposed by OMO93 remain the best set of indicators for constraining the average spectral type and luminosity class of cool evolved stars, and the amount of dilution near 1.6 μm and 2.3 μm . The W_{Ca} and W_{Mg} offer alternatives to $W_{1.62}$ and $W_{1.59}$ in the K -band.

- There is still an important need for empirical and theoretical work to further investigate metallicity effects and better constrain the stellar properties and evolution at high luminosities, including red supergiants and AGB stars. The work initiated by Origlia, Oliva and coworkers (Origlia *et al.* 1997; Oliva & Origlia 1998; Origlia & Oliva 2000) and by Lançon and her collaborators (Lançon & Wood 1998; Lançon *et al.* 1999; Alvarez *et al.* 2000) constitute valuable contributions in this direction.

I am grateful to the MPE-3D team for help with the observations. I wish to thank E. Oliva, L. Tacconi-Garman, L. Tacconi, R. Maiolino, and R. Genzel for interesting discussions and useful comments on the manuscript. I also thank the anonymous referee for further helpful comments and suggestions. This research made use of the SIMBAD database operated by CDS in Strasbourg, France. I acknowledge the Fonds pour les Chercheurs et l’Aide à la Recherche (Gouvernement du Québec, Canada) for a Graduate Scholarship, and the Max-Planck-Institut für extraterrestrische Physik as well as the Service d’Astrophysique of the CEA Saclay for additional financial support.

REFERENCES

- Ali, B., Carr, J. S., DePoy, D. L., Frogel, J. A., & Sellgren, K. 1995, *AJ*, 110, 2415
- Alvarez, R., Lançon, A., Plez, B., & Wood, P. R. 2000, *A&A*, 353, 322
- Böker, T., Förster-Schreiber, N. M., & Genzel, R. 1997, *AJ*, 114, 1883
- Bruzual A., G. & Charlot, S. 1993, *ApJ*, 405, 538
- Cayrel de Strobel, G., Hauck, B., François, P., Thévenin, F., Friel, E., Mermilliod, M., & Borde, S. 1992, *A&AS*, 95, 273
- Dallier, R., Boisson, C., & Joly, M. 1996, *A&AS*, 116, 239 (DBJ96)
- Dominy, J. F. 1984, *ApJS*, 55, 27
- Förster Schreiber, N. M., Genzel, R., Lutz, D., Kunze, D., & Sternberg, A. 2000a, *ApJ*, submitted
- Förster Schreiber, N. M., Genzel, R., Lutz, D., Sternberg, A., & Thornley, M. D. 2000b, in preparation
- Frogel, J. A., Cohen, J. G., & Persson, S. E. 1983, *ApJ*, 275, 773
- Frogel, J. A., Persson, S. E., Aaronson, M., & Matthews, K. 1978, *ApJ*, 220, 75
- Garrison, R. F. 1994, in *ASP Conf. Ser. 60, The MK Process at 50 Years: a Powerful Tool for Astrophysical Insight*, ed. C. J. Corbally, R. O. Gray, & R. F. Garrison (San Francisco: ASP), 3
- Humphreys, R. M. & McElroy, D. B. 1984, *ApJ*, 284, 565
- Johnson, H. L. & Méndez, M. E. 1970, *AJ*, 75, 785
- Keenan, P. C. 1987, *PASP*, 99, 713
- Keenan, P. C. & McNeil, R. C. 1989, *ApJS*, 71, 245
- Keenan, P. C. & Morgan, W. W. 1941, *ApJ*, 94, 501
- Keenan, P. C. & Pitts, R. E. 1980, *ApJS*, 42, 541
- Keenan, P. C. & Yorke, S. B. 1988, *Bull. D'Inf. CDS*, 35, 37
- Kleinmann, S. G. & Hall, D. N. B. 1986, *ApJS*, 62, 501 (KH86)
- Kurucz, R. L. 1979, *ApJS*, 40, 1
- Lançon, A., Mouhcine, M., Fioc, M., & Silva, D. 1999, *A&A*, 344, L21

- Lançon, A. & Rocca-Volmerange, B. 1992, *A&AS*, 96, 593
- Lançon, A. & Rocca-Volmerange, B. 1996, *New Astronomy*, 1, 215
- Lançon, A. & Wood, P. R. 1998, in *IAU Symp. 189, Fundamental Stellar Properties: the Interaction between Observations and Theory*, ed. T. R. Bedding (Publ. School of Physics, Univ. of Sydney), 168
- Leitherer, C., *et al.* 1996, *PASP*, 108, 996
- Lord, S. 1992, NASA Techn. Mem. 103957, Ames Research Center, Moffet Field, CA
- McGregor, P. J. 1987, *ApJ*, 312, 195
- McWilliam, A. 1990, *ApJS*, 74, 1075
- McWilliam, A. & Lambert, D. L. 1984, *PASP*, 96, 882
- Meyer, M. R., Edwards, S., Hinkle, K. H., & Strom, S. E. 1998, *ApJ*, 508, 397
- Morgan, W. W. & Keenan, P. C. 1973, *ARA&A*, 11, 29
- Ohnaka, K. & Tsuji, T. 1996, *A&A*, 310, 933
- Oliva, E. & Origlia, L. 1998, *A&A*, 332, 46
- Oliva, E., Origlia, L., Kotilainen, J. K., & Moorwood, A. F. M. 1995, *A&A*, 301, 55
- Oliva, E., Origlia, L., Maiolino, R., & Moorwood, A. F. M. 1999, *A&A*, 350, 9
- Origlia, L., Ferraro, F. R., Fusi Pecci, F., & Oliva, E. 1997, *A&A*, 321, 859
- Origlia, L., Moorwood, A. F. M., & Oliva, E. 1993, *A&A*, 280, 536 (OMO93)
- Origlia, L. & Oliva, E. 2000, *A&A*, 357, 61
- Ramírez, S. V., DePoy, D. L., Frogel, J. A., Sellgren, K., & Blum, R. D. 1997, *AJ*, 113, 1411
- Schmidt-Kaler, T. 1982, in *Landolt-Börnstein New Series, Vol. 2b, Astronomy and Astrophysics: Stars and Star Clusters*, ed. K. Schaifers & H. H. Voigt (New York: Springer), 451
- Shane, C. D. 1928, *Lick Obs. Bull.*, 13, 123
- Stephens, A., Frogel, J. A., & Ramírez, S. V. 2000, in preparation
- Taylor, B. J. 1991, *ApJS*, 76, 715
- Terndrup, D. M., Frogel, J. A., & Whitford, A. E. 1991, *ApJ*, 378, 742
- Thatte, N., Quirrenbach, A., Genzel, R., Maiolino, R., & Tecza, M. 1997, *ApJ*, 490, 238

- van der Hulst, J. M., Terlouw, J. P., Begeman, K., Zwitter, W., & Roelfsema, P. R. 1992, in ASP Conf. Ser. 25, *Astronomical Data Analysis Software and Systems I*, ed. D. M. Worall, C. Biemesderfer, & J. Barnes (San Francisco: ASP), 131
- Wallace, L. & Hinkle, K. 1996, *ApJS*, 107, 312
- Wallace, L. & Hinkle, K. 1997, *ApJS*, 111, 445
- Wallerstein, G. & Knapp, G. R. 1998, *ARA&A*, 36, 369
- Weitzel, L., Krabbe, A., Kroker, H., Thatte, N., Tacconi-Garman, L. E., Cameron, M., & Genzel, R. 1996, *A&AS*, 119, 531
- Worthey, G. 1994, *ApJS*, 95, 107
- Yamashita, Y. 1972, *Ann. Tokyo Astron. Obs. Sec. Ser.*, 13, 169

Fig. 1.— 3D spectra at $R \approx 830$: (a) giants, and (b) supergiants. The spectra are normalized to unity between $2.2875 \mu\text{m}$ and $2.2910 \mu\text{m}$. In each panel, the vertical axis is the appropriate flux scale for the bottom spectrum and each successive spectrum is shifted upwards by 0.5. The strongest features longwards of $2.15 \mu\text{m}$ are labeled, following the nomenclature of Kleinmann & Hall (1986).

Fig. 2.— 3D spectra at $R \approx 2000$: (a) giants, (b) supergiants, and (c) carbon stars. The spectra are normalized to unity between $2.2875 \mu\text{m}$ and $2.2910 \mu\text{m}$. In each panel, the vertical axis is the appropriate flux scale for the bottom spectrum and each successive spectrum is shifted upwards by 0.5. The strongest features longwards of $2.15 \mu\text{m}$ are labeled, following the nomenclature of Kleinmann & Hall (1986).

Fig. 3.— Comparison of the spectra of the carbon stars (black lines) with those of normal giants of similar effective temperature (grey lines). The spectra are normalized and displayed on a linear flux scale as for figure 1.

Fig. 4.— Comparison of a subset of 3D spectra at $R \approx 2000$ (black lines) with spectra of stars having similar spectral types from Kleinmann & Hall (1986), convolved to the resolution of the 3D data (grey lines). The latter have been multiplied by a power law continuum proportional to $\lambda^{-3.94}$ in order to recover the original energy distribution of the stars (see section 3.1). All spectra are normalized and displayed on a linear flux scale as for figure 1.

Fig. 5.— Variations with stellar effective temperature of the equivalent widths of the atomic and molecular absorption features discussed in the text. Open symbols represent data for supergiants and carbon stars, filled symbols represent data for giants, and crosses represent data for dwarfs. Different symbols are also used to distinguish between data from various authors, as indicated in the insets (3D: this work; KH86: Kleinmann & Hall 1986; OMO93: Origlia *et al.* 1993; DBJ96: Dallier *et al.* 1996). The typical measurement uncertainties are $\pm 0.5 \text{ \AA}$ for the atomic features and $W_{1.62}$, $\pm 0.8 \text{ \AA}$ for $W_{2.29}$, and $\pm 1.0 \text{ \AA}$ for $W_{2.32}$ and $W_{2.34}$.

Fig. 6.— Positions of the lines of various species contributing to the K -band atomic features considered in this work, as identified by Wallace & Hinkle (1996) in $R \geq 45000$ spectra of red dwarfs, giants, and supergiants. The bandpasses used to integrate the depth of the atomic features are indicated on the spectrum of HD 120323 by the dotted lines (see table 3).

Fig. 7.— Variations of composite spectroscopic indices with stellar effective temperature. The symbols are the same as for figure 5, and labeled in the insets. Data of dwarfs are shown for $W_{2.29}/(W_{\text{Ca}} + W_{\text{Na}})$ to illustrate that this indicator is a less powerful discriminator between giants and supergiants than it is between dwarfs and giants (see section 4.2). The sharp increase of $W_{2.29}/W_{2.34}$ at high T_{eff} likely is an artefact reflecting the extreme weakness of the $^{13}\text{CO}(2,0)$ bandhead.

Fig. 8.— Diagnostic diagrams for estimating the amount of dilution of the stellar absorption features by excess continuum emission. The composite indices used for the horizontal axes are sensitive to T_{eff} only. The arrows show the effects on the indices of dilution near $1.6\ \mu\text{m}$ (top left panel) and near $2.3\ \mu\text{m}$ (other panels). The symbols are the same as for figure 5, and labeled in the insets.

Table 1. Program stars

Star	Spectral type	References	[Fe/H] ^a	References
HD 44030	K4 II	1	−0.22; −0.7	4; 1
HD 78647	K4.5 Ib	2	0.23	1
HD 35601	M1.5 Iab-Ib	2	−0.24	1
HD 36389	M2 Iab-Ib	2	0.11	1
HD 94613	M3+ Ib	2
HD 90382	M3.5 Iab	2
HD 20791	G8.5 III	2
HD 62509	K0 IIIb	2	0.01; −0.07; −0.51 to 0.16	4; 5; 1
HD 74442	K0 IIIb	2	−0.11; −0.13	4; 5
HD 37160	K0 IIIb Fe-2	2	−0.58; −0.63; −0.70 to −0.19	4; 5; 1
HD 49293	K0+ IIIa	2	−0.08; −0.12	4; 5
HD 107328	K0.5 IIIb Fe-0.5	2	−0.32; −0.48; −0.64 to −0.12	4; 5; 1
HD 89484	K1− IIIb Fe-0.5	2	−0.25; −0.49; −0.41 to 0.09	4; 5; 1
HD 85859	K2.5 III	2	−0.08; −0.03	4; 5
HD 34334	K2.5 III Fe-1	2	−0.26; −0.46; −0.39, −0.25	4; 5; 1
HD 97907	K3 III	1	−0.09	4
HD 90432	K4+ III	2	−0.24; −0.12	4; 5
HD 133774	K5− III	2	−0.41; 0.01	4; 5
HD 82668	K5 III	2
HD 29139	K5+ III	2	−0.16; −0.34; −0.33 to 0.00	4; 5; 1
HD 95578	M0 III	2
HD 80874	M0.5 III	2
HD 25025	M0.5 IIIb Ca-1	2
HD 102212	M1 III	2	−0.09	1
HD 119149	M1.5 III	2
HD 120052	M2 III	2
HD 44478	M3 IIIab	2	−0.05	1
HD 80431	M4 III	2
HD 4408	M4 IIIa	2
HD 102620	M4+ III	2
HD 120323	M4.5 III	2
HD 113801	C2,1 (R0)	3	−0.26	1
HD 92055	C6,3 (N2)	3	−0.1	1

References. — 1: Cayrel de Strobel *et al.* (1992); 2: Keenan & McNeil (1989); 3: Yamashita (1972); 4: Taylor (1991); 5: McWilliam (1990).

^a Metallicities are averages computed by Taylor (1991) from data in the literature, values collected from the literature compiled by Cayrel de Strobel *et al.* (1992), and best fits to high resolution optical spectra and photometric data using model atmospheres by McWilliam (1990).

Table 2. Log of the observations

Star	$t_{\text{int}}^{\text{a}}$ (s)	Calibrator	Run ^b	Range (μm)	R	est. S/N ^c
HD 44030	100	PPM 95062 (F8 V)	CA95	1.90 – 2.40	830	376
HD 78647	10	BS 3699 (A8 Ib)	LS96	2.18 – 2.45	2000	113
HD 35601	54	PPM 95062 (F8 V)	CA95	1.90 – 2.40	830	205
HD 36389	4.5	PPM 95062 (F8 V)	CA95	1.90 – 2.40	830	213
HD 94613	38	HD 87504 (B9 III-IV)	LS96	2.18 – 2.45	2000	99
HD 90382	40	BS 4037 (B8 IIIe)	LS96	2.18 – 2.45	2000	85
HD 20791	112	BS 1153 (B3 V)	LP96	1.90 – 2.40	830	328
HD 62509	2.7	BS 2890 (A2 V)	CA95	1.90 – 2.40	830	218
HD 74442	14.5	BS 3510 (G1 V)	LP96	1.90 – 2.40	830	309
HD 37160	95	PPM 95062 (F8 V)	CA95	1.90 – 2.40	830	343
HD 49293	36	BS 2779 (F8 V)	CA95	1.90 – 2.40	830	277
HD 107328	40	BS 4757 (B9.5 V)	LS96	2.18 – 2.45	2000	112
HD 89484	49	BS 4039 (F8 V)	CA95	1.90 – 2.40	830	212
HD 85859	95	HD 71459 (B3 V)	LS96	2.18 – 2.45	2000	108
HD 34334	58	PPM 95062 (F8 V)	CA95	1.90 – 2.40	830	349
HD 97907	140	PPM 158259 (F8 V)	CA95	1.90 – 2.40	830	418
HD 90432	38	HD 87504 (B9 III-IV)	LS96	2.18 – 2.45	2000	155
HD 133774	20	HD 136664 (B4 V)	LS96	2.18 – 2.45	2000	107
HD 82668	9.5	HD 87504 (B9 III-IV)	LS96	2.18 – 2.45	2000	83
HD 29139	8.7	BS 788 (F9 V)	CA95	1.90 – 2.40	830	323
HD 95578	9	HD 87504 (B9 III-IV)	LS96	2.18 – 2.45	2000	119
HD 80874	19	HD 71459 (B3 V)	LS96	2.18 – 2.45	2000	112
HD 25025	14.5	BS 788 (F9 V)	CA95	1.90 – 2.40	830	283
HD 102212	49	PPM 158259 (F8 V)	CA95	1.90 – 2.40	830	328
HD 119149	40	HD 129116 (B3 V)	LS96	2.18 – 2.45	2000	100
HD 120052	19	HD 129116 (B3 V)	LS96	2.18 – 2.45	2000	132
		BS 4134 (F6 V)				
HD 44478	2.7	PPM 95062 (F8 V)	CA95	1.90 – 2.40	830	344
HD 80431	100	BS 3836 (A5 IV-V)	LS96	2.18 – 2.45	2000	142
HD 4408	22.2	HD 4676 (F8 V)	LP96	1.90 – 2.40	830	290
HD 102620	6	BS 4662 (B8 IIIpHgMn)	LS96	2.18 – 2.45	2000	133
HD 120323	9.5	BS 4979 (G3 V)	LS96	2.18 – 2.45	2000	99
HD 113801	600	BS 5210 (B5 III)	LS96	2.18 – 2.45	2000	82
HD 92055	10	BS 3836 (A5 IV-V)	LS96	2.18 – 2.45	2000	25

^a Total on-source integration time per wavelength channel.

^b CA95 : January 1995 run at the 3.5 m telescope at Calar Alto, Spain; LS96 : April 1996 run at the ESO 2.2 m telescope at La Silla, Chile. LP96 : January 1996 run at the 4.2 m William-Herschel-Telescope on the Canary Islands, Spain;

^c Estimated signal-to-noise ratio per wavelength channel evaluated on the reduced spectra between 2.242 μm and 2.258 μm (see section 2.3).

Table 3. Continuum points and bandpass edges for the absorption features

Feature	Symbol	Continuum points ^a (μm)	Integration limits (μm)
Si I 1.5892 μm	$W_{1.59}$	1.5850, 1.5930	1.5870 – 1.5910
^{12}CO (6,3) 1.6187 μm	$W_{1.62}$	1.6160, 1.6270	1.6175 – 1.6220
Na I 2.2076 μm	W_{Na}	2.1965, 2.2125, 2.2175	2.2053 – 2.2101
Fe I 2.2263 μm	W_{Fe1}	2.2125, 2.2175, 2.2323	2.2248 – 2.2293
Fe I 2.2387 μm	W_{Fe2}	2.2323, 2.2510, 2.2580	2.2367 – 2.2402
Ca I 2.2636 μm	W_{Ca}	2.2510, 2.2580, 2.2705, 2.2760	2.2611 – 2.2662
Mg I 2.2814 μm	W_{Mg}	2.2705, 2.2760, 2.2900	2.2788 – 2.2840
^{12}CO (2,0) 2.2935 μm	$W_{2.29}$	2.2900	2.2924 – 2.2977
^{12}CO (3,1) 2.3227 μm	$W_{2.32}$	2.2125, 2.2175, 2.2335, 2.2580, 2.2705, 2.2900	2.3218 – 2.3272
^{13}CO (2,0) 2.3448 μm	$W_{2.34}$	(same as for $W_{2.32}$)	2.3436 – 2.3491

^a Central wavelength of the 0.002 – 0.003 μm wide intervals used to fit the normalizing continuum.

Table 4. Measured equivalent widths

Star	Type	W_{Na}	W_{Fe1}	W_{Fe2}	W_{Ca}	W_{Mg}	$W_{2.29}$	$W_{2.32}$	$W_{2.34}$
HD 44030	K4 II	2.7	1.7	...	12.0	13.0	9.6
HD 78647	K4.5 Ib	3.1	2.1	1.4	2.5	1.0	15.3	15.0	9.7
HD 35601	M1.5 Iab-Ib	4.2	2.9	...	19.7	22.0	14.7
HD 36389	M2 Iab-Ib	4.6	3.1	...	19.2	21.8	15.4
HD 94613	M3+ Ib	4.7	2.8	1.5	2.7	1.2	20.0	21.8	12.7
HD 90382	M3.5 Iab	5.0	3.3	2.0	3.7	1.3	19.6	20.9	14.5
HD 20791	G8.5 III	1.4	1.1	...	5.1	5.8	1.6
HD 62509	K0 IIIb	1.3	1.1	...	5.5	5.9	1.8
HD 74442	K0 IIIb	1.8	1.5	...	7.6	8.2	4.4
HD 37160	K0 IIIb Fe-2	1.3	0.9	...	6.0	6.4	1.8
HD 49293	K0+ IIIa	2.3	1.7	...	7.8	8.6	3.0
HD 107328	K0.5 IIIb Fe-0.5	1.5	0.7	0.5	1.0	0.9	10.3	10.1	6.5
HD 89484	K1– IIIb Fe-0.5	2.3	1.3	...	8.5	9.5	5.3
HD 85859	K2.5 III	2.2	0.9	0.4	1.6	1.0	9.7	9.7	5.1
HD 34334	K2.5 III Fe-1	2.0	1.4	...	9.8	11.0	6.9
HD 97907	K3 III	2.5	1.8	...	9.1	10.5	5.3
HD 90432	K4+ III	2.6	1.7	1.0	2.1	0.9	11.4	11.3	7.8
HD 133774	K5– III	2.9	1.9	1.2	2.8	1.2	12.8	11.8	7.3
HD 82668	K5 III	2.1	1.3	0.8	2.2	0.5	11.9	11.5	8.1
HD 29139	K5+ III	2.7	2.2	...	12.2	11.3	8.0
HD 95578	M0 III	3.0	1.6	0.9	2.7	1.1	13.6	12.7	8.4
HD 80874	M0.5 III	3.0	1.8	1.1	2.6	1.1	13.6	13.5	9.9
HD 25025	M0.5 IIIb Ca-1	3.1	2.0	...	12.5	12.4	8.5
HD 102212	M1 III	2.5	2.3	...	12.1	12.6	10.0
HD 119149	M1.5 III	3.5	2.3	1.3	2.8	0.7	14.2	13.2	9.8
HD 120052	M2 III	2.3	1.2	0.7	2.6	0.6	13.1	12.5	10.2
HD 44478	M3 IIIab	3.5	2.5	...	13.5	14.3	11.2
HD 80431	M4 III	3.2	2.4	1.3	3.2	1.1	16.3	14.7	11.7
HD 4408	M4 IIIa	3.3	3.3	...	14.9	16.5	12.2
HD 102620	M4+ III	3.5	2.2	1.5	3.4	0.9	15.2	14.8	12.3
HD 120323	M4.5 III	3.7	1.9	1.1	3.9	1.5	13.5	11.6	10.2
HD 113801	C2,1 (R0)	9.8	10.1	3.6
HD 92055	C6,3 (N2)	17.5	16.8	13.1

Note. — The equivalent widths are given in Å. The typical measurement uncertainties are ± 0.5 Å for the atomic features, ± 0.8 Å for $W_{2.29}$, and ± 1.0 Å for $W_{2.32}$ and $W_{2.34}$.

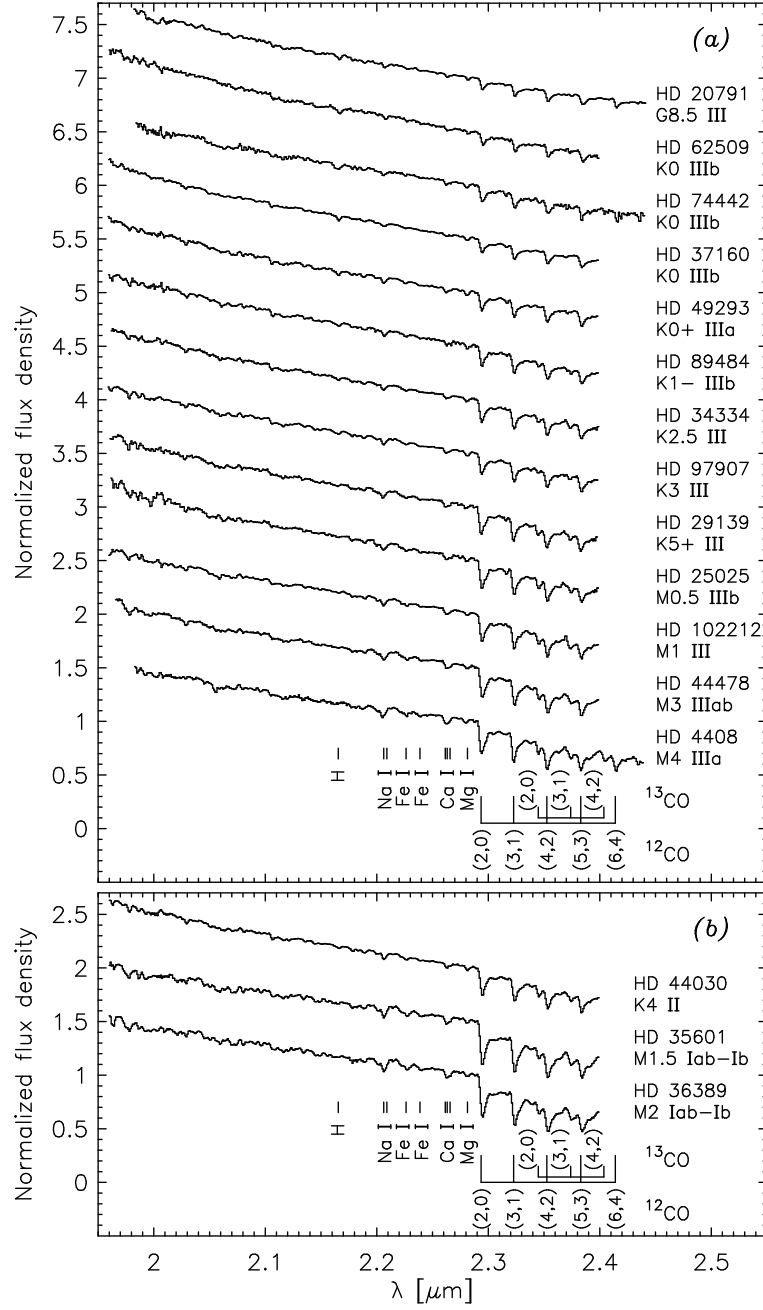


Fig. 1.—

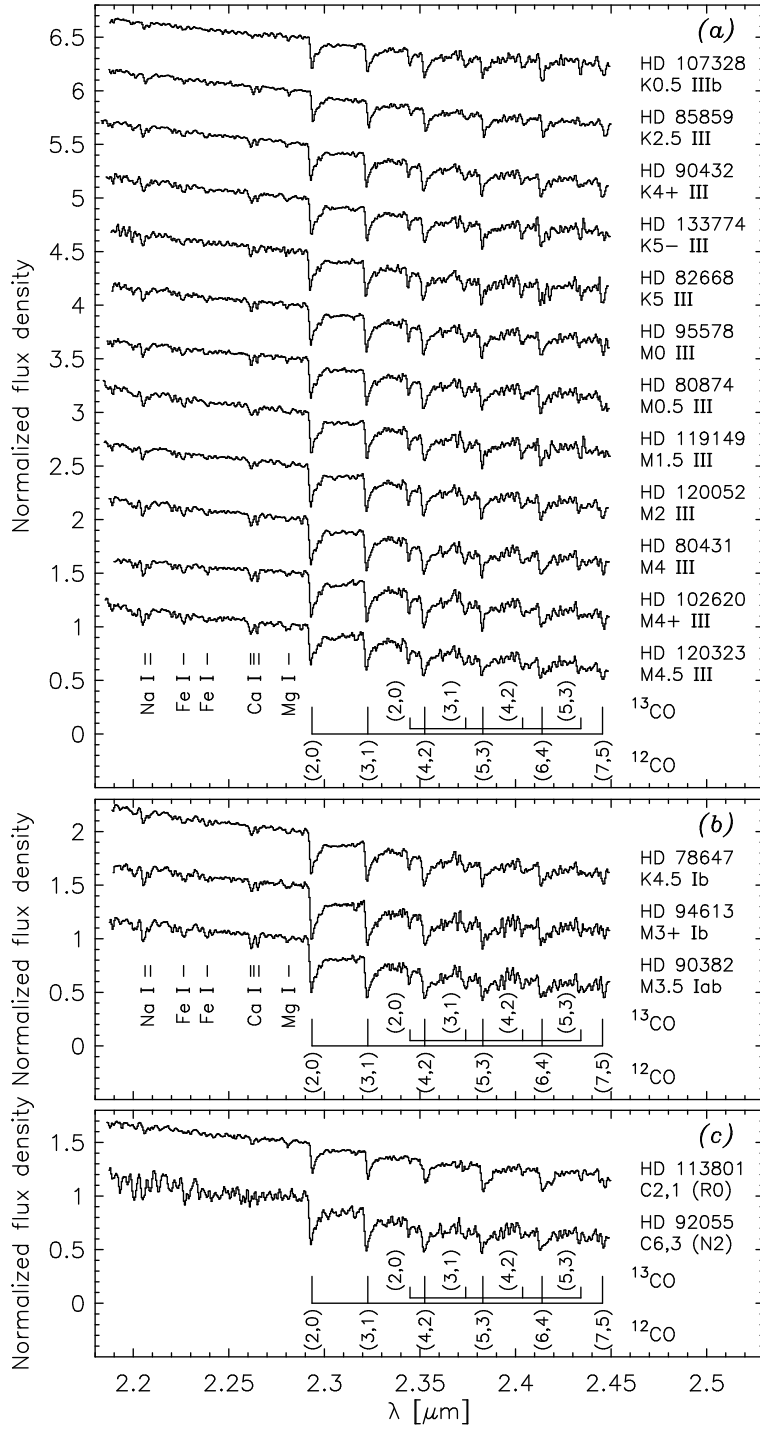


Fig. 2.—

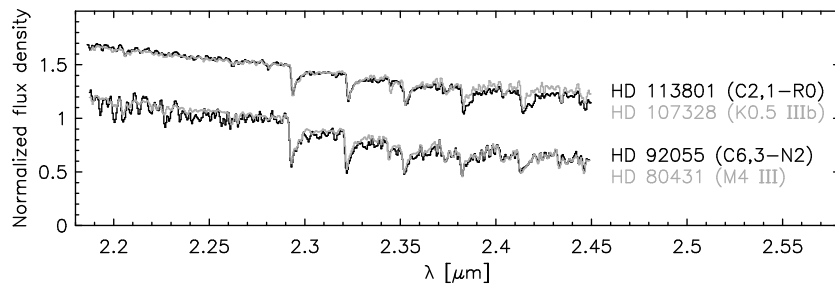


Fig. 3.—

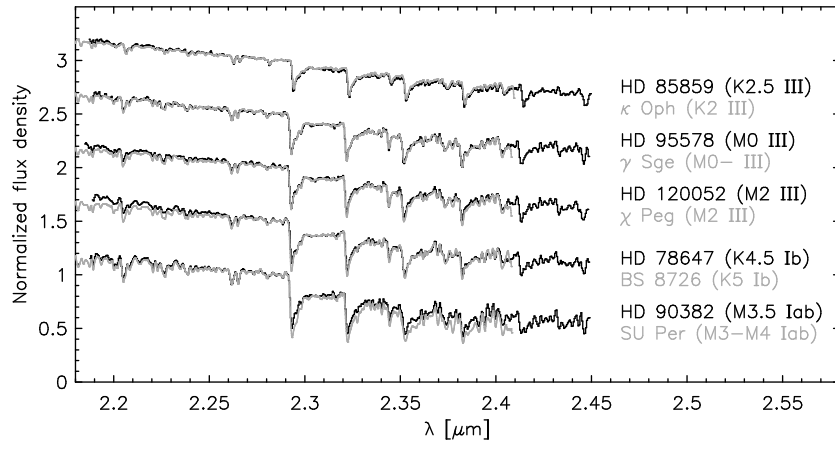


Fig. 4.—

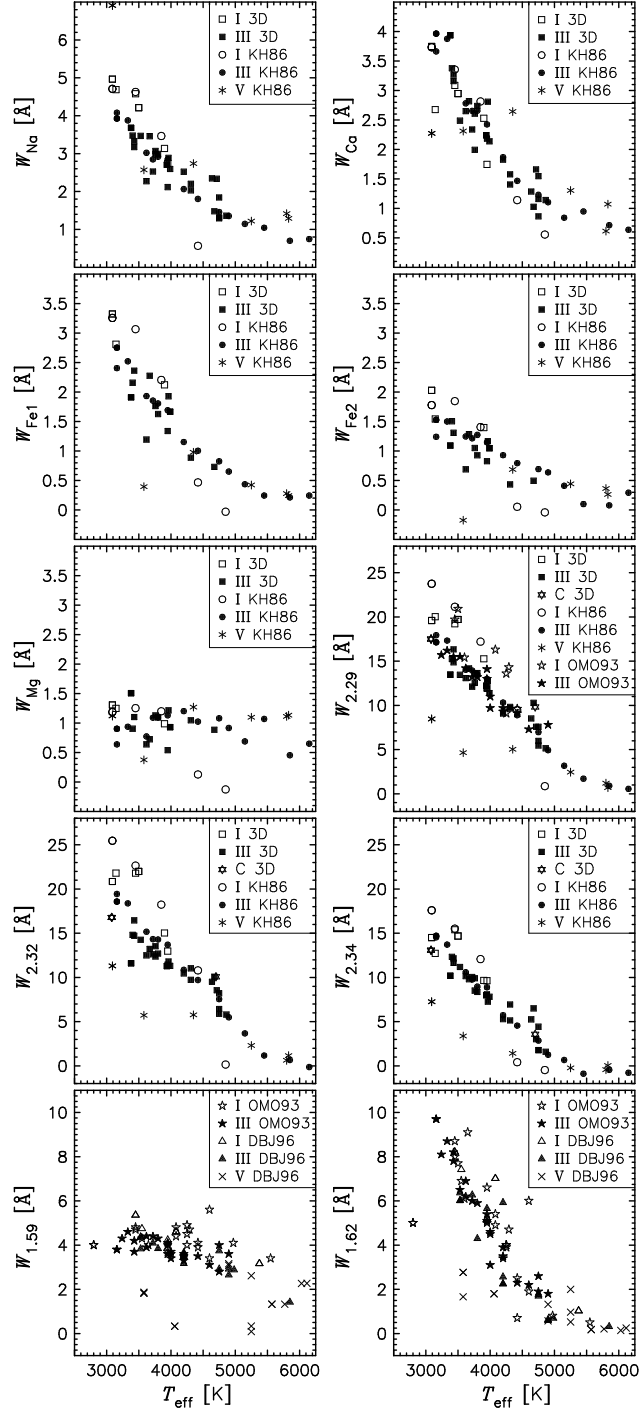


Fig. 5.—

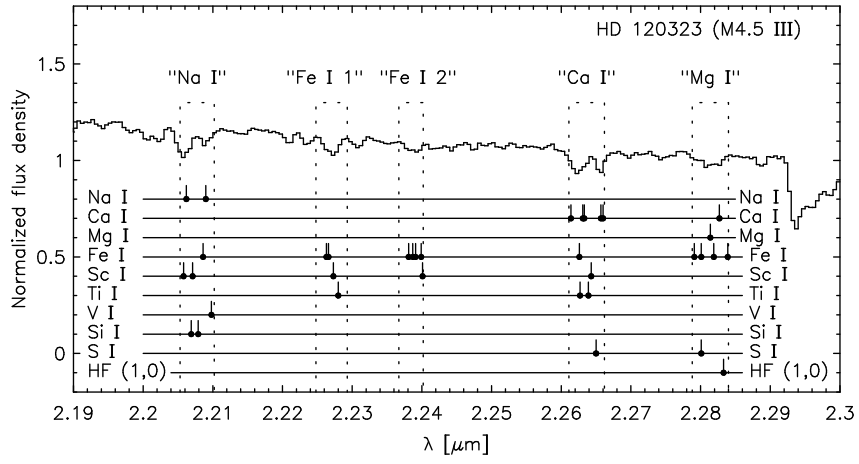


Fig. 6.—

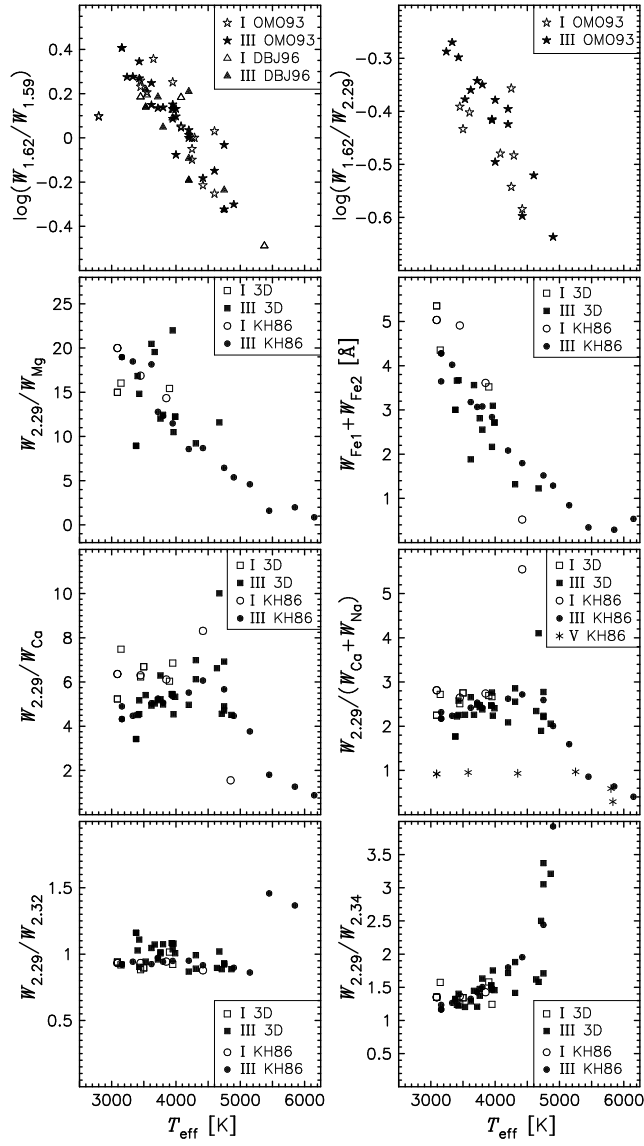


Fig. 7.—

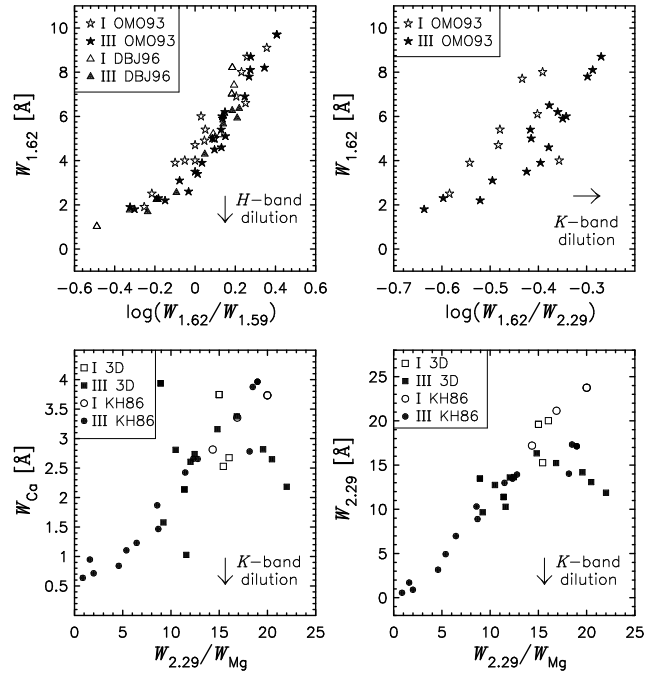


Fig. 8.—